Magneto-Optical Nanoparticles for Cyclic Magnetomotive Photoacoustic Imaging

Junwei Li,[‡] Bastien Arnal,[‡] Chen-Wei Wei,[‡] Jing Shang, Thu-Mai Nguyen, Matthew O'Donnell,[*] and Xiaohu Gao[*]

Department of Bioengineering, University of Washington, Seattle, Washington 98195, United States. [‡]These authors contributed equally.

ABSTRACT Photoacoustic imaging has emerged as a highly promising tool to visualize molecular events with deep tissue penetration. Like most other modalities, however, image contrast under *in vivo* conditions is far from optimal due to background signals from tissue. Using iron oxide—gold core—shell nanoparticles, we have previously demonstrated the concept of magneto-motive photoacoustic (mmPA) imaging, which is capable of dramatically reducing the influence of background signals and producing high-contrast molecular images. Here, we report two significant advances toward clinical translation of this technology. First, we introduce a new class of compact, uniform, magneto-optically coupled core—shell nanoparticles, prepared through localized copolymerization of polypyrrole (PPy) on an iron oxide nanoparticle surface. The resulting iron oxide—PPy nanoparticles feature high colloidal stability and solve the photoinstability and small-scale synthesis problems previously encountered by the gold coating approach. In parallel, we have developed a new generation of mmPA featuring cyclic magnetic motion and ultrasound speckle tracking (USST), whose imaging capture frame rate is several hundred times faster than the photoacoustic speckle tracking (PAST) method we demonstrated previously. These advances enable robust artifact elimination caused by physiologic motions and demonstrate the application of the mmPA technology for *in vivo* sensitive tumor imaging.

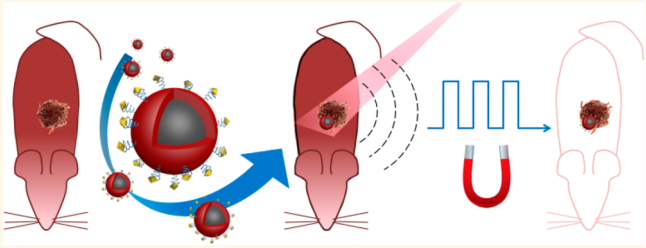

KEYWORDS: nanoparticles · photoacoustic imaging · magnetic · near-infrared · cancer · diagnosis · multifunctional · polypyrrole

Deadly diseases such as metastatic cancer are difficult to cure. For many types of cancer, however, the chances of treating them effectively are actually very good if precancerous lesions or the primary tumors, before they metastasize, can be detected early.[1] Along with biomarker screening, imaging is one of the most important elements of cancer detection and staging, and advanced molecular imaging techniques can potentially allow direct visualization of cellular functions and molecular processes in small lesions. Unfortunately, current imaging modalities suffer both poor sensitivity and specificity under *in vivo* conditions. On the biology side, biomarkers with high specificity to diseased cells are urgently needed, whereas on the imaging side, approaches to improve contrast remain a major challenge. Regardless of the modality, a common problem for noninvasive imaging is the strong background signals from tissue. For example, in optical imaging, photon absorption, scattering, and autofluorescence obscure specific signals from targeted contrast agents. Similarly, for magnetic resonance imaging, specific signals from contrast agents attached to targeted cells are often overwhelmed by background signals due to the high water content of the human body.

We recently demonstrated an innovative concept to suppress intrinsic background signals using photoacoustic imaging as a model system.[2] Photoacoustic imaging combines pulsed laser irradiation of a contrast agent with ultrasound detection of the resulting thermally induced acoustic waves. Currently, exogenous contrast agents for photoacoustic imaging are based on efficient light absorbers such as inorganic nanstructures, small-molecule near-infrared (NIR) dyes, and conjugated polymers.[3−6] Although tissues are not as efficient as the contrast agent in terms of light absorption, the concentration of targeted agent is

* Address correspondence to odonnel@uw.edu, xgao@uw.edu.

Received for review December 4, 2014 and accepted February 3, 2015.

Published online February 06, 2015
10.1021/nn5069258

usually low *in vivo* and may be easily masked by strong background signals. To solve this problem, a new technique, magnetomotive photoacoustic (mmPA), was proposed previously.[2] It uses magneto-optical nanoparticles composed of a core magnetic nanoparticle and a gold nanoshell, enabling magnetic manipulation with simultaneous photoacoustic detection. Theoretically, cancer cells tagged with the core–shell nanoparticles could be magnetically moved (through the magnetic core) with an external magnetic field. This movement would modulate photoacoustic signals (generated by the nanoshell) spatially, enabling subsequent motion filtering on a series of recorded photoacoustic signals to suppress magnetically insensitive background signals. Using nanoparticles embedded in a phantom of similar elasticity to tissues, the contrast can be improved by 1–3 orders of magnitude over conventional photoacoustic imaging,[2] making both sensitive and specific detection of small lesions possible.

Although mmPA represents an attractive approach for molecular imaging, several fundamental and practical issues must be addressed to promote rapid translation of the technology to the clinic. First, because mmPA utilizes motion to suppress background signals, it is critically important to avoid artifacts caused by physiologic motion such as cardiac-induced motion and respiration. Second, photoacoustic imaging signals are generated by repeated irradiation of contrast agents by high-intensity pulsed lasers. To minimize light absorption and scattering by biological tissue, wavelengths in the NIR spectrum are highly preferred (e.g., 800 nm). A number of inorganic metallic nanostructures such as gold nanorods, nanoshells, and nanocages have been developed for this purpose because of their tunable absorption spectra. Unfortunately, these nanostructures are thermodynamically unstable and prone to photoinduced degradation. Using the most popular photoacoustic contrast agent, gold nanorods, as an example, under pulsed laser irradiation, they melt into spherical particles of similar volumes or even fragment into smaller particles.[7–9] Previously, silica encapsulation has been shown to improve gold nanorods' photostability[10,11] but at the expense of significantly increased particle size. Therefore, novel contrast agents stable under intense pulsed-laser illumination must be developed. In addition to these fundamental issues, some practical issues must also be addressed for clinical translation. The leading one is the scalability of nanoprobe synthesis. Large quantities of agent must be produced with a cost-effective process to enable routine clinical use of any molecular imaging approach.

Here, we report a comprehensive solution to these requirements by developing a new class of compact, uniform, NIR-responsive, and magnetic contrast agent composed of a core magnetic nanoparticle (MNP) and a shell of conducting polymers (polypyrrole (PPy), Figure 1a). In parallel, to accelerate potential clinical translation, we developed the next generation of mmPA imaging by introducing multicycle magnetic motion (Figure 1b) and coupling photoacoustic imaging with ultrasound speckle tracking (USST). Previously, contrast enhancement based on the absolute amplitude of spatial displacement has been explored by us (first generation mmPA) and others, but these techniques based on single-cycle displacement magnitude thresholding are intrinsically sensitive to physiological motion.[2,12] Cyclic mmPA (cmmPA), based on signal time coherence, is significantly more robust in distinguishing true magnetomotion from physiological motion artifacts. More importantly, besides speckle tracking performed with photoacoustic images, we show that the estimation of magnetically induced displacement in the new mmPA technology can be obtained with a series of ultrasound (US) images at kHz frame rates, hundreds of times faster than photoacoustic imaging's frame rate determined by the current laser repetition rate (10 Hz). These advances enable the first demonstration of mmPA *in vivo*.

RESULTS AND DISCUSSION

A number of attempts have been reported to make MNP–PPy core–shell nanoparticles due to their attractive properties and potential impact on biosensing, -imaging, and photothermal therapy. Relatively large particles (submicron) coated with conjugated polymers have been made with uniform size and shell thickness and clear observation of the core–shell structures.[13,14] Unfortunately, these particles are too big for efficient receptor-mediated endocytosis (optimal size of ~50 nm)[15] and *in vivo* vascular extravasation, particularly for hypopermeable disease sites.[16] Compact MNP–PPy composite nanoparticles with uniform size, good colloidal stability, and balanced magnetization and NIR absorption are difficult to achieve simultaneously. Dr. Liu and co-workers recently demonstrated the synthesis of uniform core–shell iron oxide@PPy using MNP clusters as the core,[17] whereas the majority of previous reports using a single magnetic nanoparticle core yield MNP–PPy hybrid particles with poor size distribution and indirect proof of the core–shell internal structure.[18–28] This is not too surprising since polymer shell formation on a preformed nanoparticle core made from different materials (seeded polymerization) is in direct competition with homogeneous nucleation and growth of the shell material. We solved this problem by promoting Py polymerization on nanoparticle surfaces and suppressing formation of pure PPy nanoparticles.

Figure 1a schematically illustrates the key steps in the synthesis of MNP–PPy core–shell nanoparticles. Highly monodisperse oleic acid-coated MNPs of 40–50 nm diameter are first solubilized into aqueous

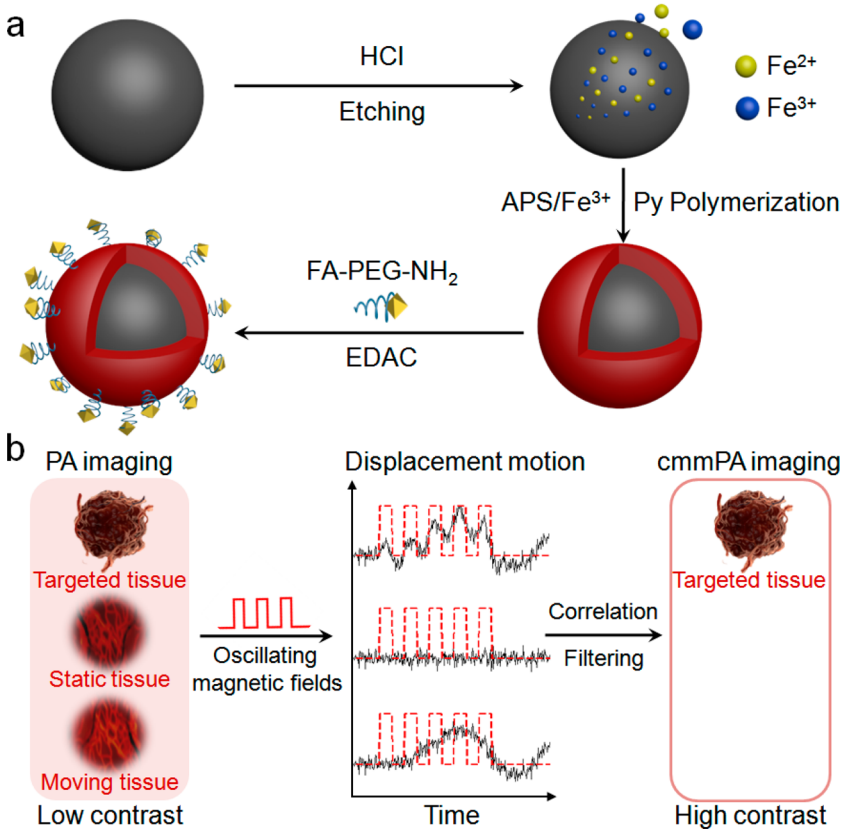

Figure 1. Schematic of MNP−PPy core−shell nanoparticle fabrication and the mechanism of cyclic mmPA in imaging contrast enhancement. (a) Key steps involved in hybrid nanoparticle synthesis: Fe^{2+}/Fe^{3+} generation though acid etching of monodisperse MNPs, PPy shell formation in the presence of Fe^{3+} and APS, and conjugation of FA−PEG−NH_2 to nanoparticle surface. (b) Schematic of tumor detection via cyclic mmPA imaging. Contrast enhancement of tumor/background by suppressing both signals from static tissues and regions with random motions from moving tissues not related to the frequency of oscillating magnetic fields while identifying specific tumor signals from targeted tissues coherently responsive to cyclic magnetic motions.

solution using an amphiphilic polymer and further stabilized with sodium dodecyl sulfate (SDS). The pH of the solution is adjusted to 2−3 using HCl to slowly etch the MNPs to generate iron ions, which have been shown to catalyze conjugated polymer polymerization.[29] Pyrrole and pyrrole-3-carboxylic acid (Py-COOH, to improve solubility and provide reactive sites) are added to the MNP solution and oxidized into a shell of polypyrrole on the MNP surface in the presence of an oxidizing reagent $(NH_4)_2S_2O_8$ (APS) (Figure 2a). The resulting core−shell magneto-optical nanoparticles are purified with magnetic separation (to remove free PPy nanoparticles), pegylated to reduce nonspecific binding, and functionalized with a targeting ligand. In this work, folic acid (FA) is used as a model to recognize a human cervical cancer cell line, HeLa.

Transmission electron microscopy (TEM) measurements clearly show the core−shell structure of MNP−PPy nanoparticles (Figure 2c). The PPy nanoshells show petal-like shell structures with a thickness ranging between 0 and 20 nm. Although the PPy shell is not perfectly spherical and smooth, it does not affect its intended use, an efficient NIR light absorber. In comparison with the original MNP, the size of the iron oxide core reduces from 47.5 ± 7.0 to 35.5 ± 8.6 nm, as a result of acid etching. Dynamic light scattering (DLS) measurements show that the hydrodynamic diameter of the core−shell nanoparticles is 51.1 ± 7.5 nm, an excellent size range for efficient endocytosis and deep tissue penetration.[15,16] Moreover, DLS also confirmed their narrow size distribution with a polydispersity index of 0.18 ± 0.01. Copolymerization of Py and Py−COOH improves the solubility and colloidal stability of the resulting nanoparticles. As shown in Figure 2b, MNP−PPy made from polymerization of pure Py forms aggregates in phosphate buffered saline (PBS) and precipitates out of solution in a few hours, whereas MNP−PPy made from copolymerization of Py and Py−COOH remains stable. The PPy nanoshell formation is further confirmed by the absorption spectrum. Strong light extinction was observed around 470 nm, indicating formation of the polymer shell. Compared to the typical bipolaron absorption peak of pure PPy centered at 480 nm, the slight spectral blue-shift is likely due to the incorporation of Py−COOH (11% by molar ratio) in the copolymer. Compared with the original MNPs, the core−shell nanoparticles show a broad absorption profile in the

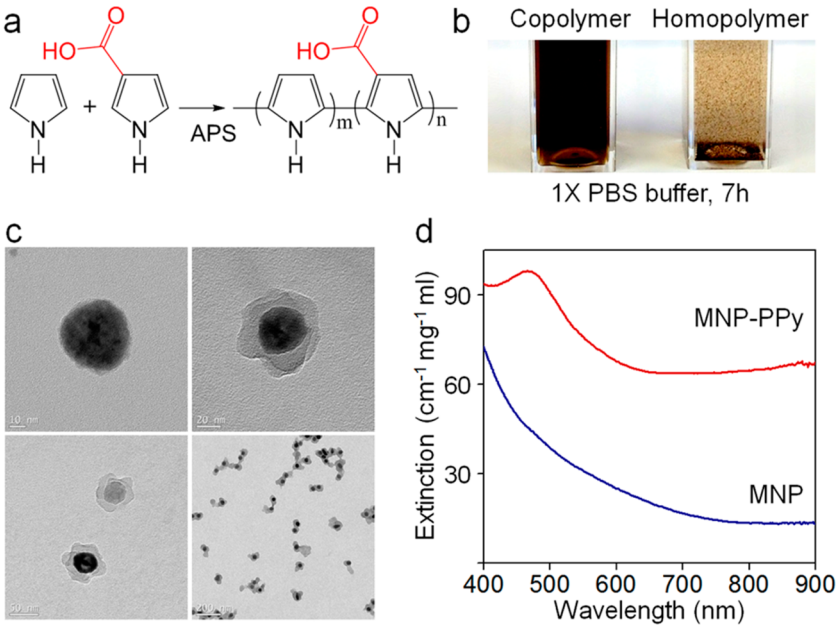

Figure 2. Preparation and characterization of the MNP−PPy hybrid nanoparticles. (a) Construction of nanoparticle shells via copolymerization of Py and Py−COOH monomers catalyzed by APS. (b) Photograph of MNP−PPy hybrid nanoparticles dispersed in 1× phosphate buffered saline (PBS) solution after 7 h (Left: copolymerization of Py and Py−COOH with 8:1 molar ratio; Right: homopolymerization of Py). (c) TEM images of the MNPs (47.5 ± 7.0 nm) and typical MNP−PPy core−shell nanoparticles (core: 35.5 ± 8.6 nm; shell: 15−25 nm) at low and high magnification. (d) Absorption spectra of MNP−PPy hybrid nanoparticles (red) and MNPs (blue) after being isolated from their respective solutions.

NIR region (Figure 2d), highly desirable for absorption-based applications such as photoacoustic imaging and photothermal therapy. At equal weight concentration, the extinction profile of MNP−PPy is 4.8 times stronger than that of MNP at 800 nm. Because light extinction comprises absorption (which really matters for PA) and scattering, we further measured the photoacoustic signal strength, which is linearly related to the nanoparticles' wavelength-dependent absorption profile (Figure S1, Supporting Information). At 800 nm, the photoacoustic signal generated by the MNP−PPy nanoparticles is 10 times stronger than that generated by MNP. This larger difference could be attributed to the absorption's dominance of the MNP−PPy overall extinction.

Under the current reaction conditions, both Fe^{3+} ions leached from the MNP surface and the added APS can serve as the oxidant for Py polymerization. In the absence of an anionic surfactant, SDS, APS is significantly more effective in PPy formation, measured by absorbance at 800 nm (Figure 3a). This is expected since APS is of higher oxidation potential than Fe^{3+}.[30] Addition of MNPs to the reaction only slightly increases the rates for both APS and Fe^{3+} oxidized polymerization (Figure 3b). Interestingly, however, addition of SDS completely reverses the efficiencies of the two reactions (Figure 3c). The reaction yield of Fe^{3+} oxidized polymerization increases by 40 times (10 h reaction time) and that for APS-based polymerization decreases by 3 times. These reaction rate changes are in agreement with previous research and have been attributed

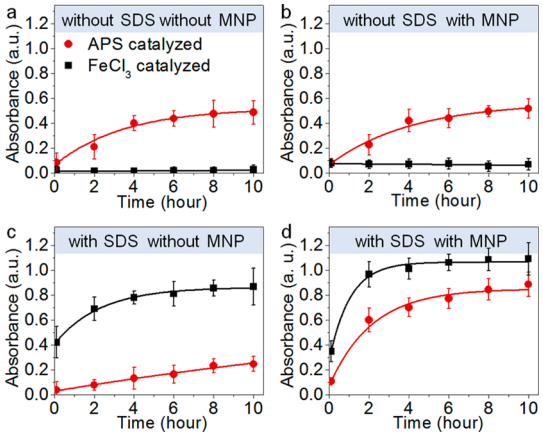

Figure 3. Kinetics of Py polymerization for eight reaction conditions. Eight individual vials containing the same amount of water (pH 2.5, 4.5 mL), Py monomers (20 mM, 450 μL), sodium dodecyl sulfate (SDS; 120 mM, 300 μL), MNPs (70 nM, 60 μL), or equally the same amount of water (control groups) prepared for polymerization. APS (2 mM, 4.5 mL) or $FeCl_3$ (4 mM, 4.5 mL) catalyzed the four vial reaction at the same time. Polymerization yield (PPy absorbance at 800 nm) is plotted as a function of time for eight conditions: (a) without SDS, without MNP; (b) without SDS, with MNP; (c) with SDS, without MNP; (d) with SDS, with MNP added inside the initial prepared solutions catalyzed by APS (red) or $FeCl_3$ (black), respectively. Concentration of $FeCl_3$ is twice as much as that of APS due to APS 2-fold higher valence than $FeCl_3$. Error bars represent standard deviations of three separate measurements.

to electrostatic attraction between negatively charged SDS and Fe^{3+} and the increased solution viscosity.[31,32] On the basis of these observations, synthesis of MNP−PPy core−shell particles can be rationally

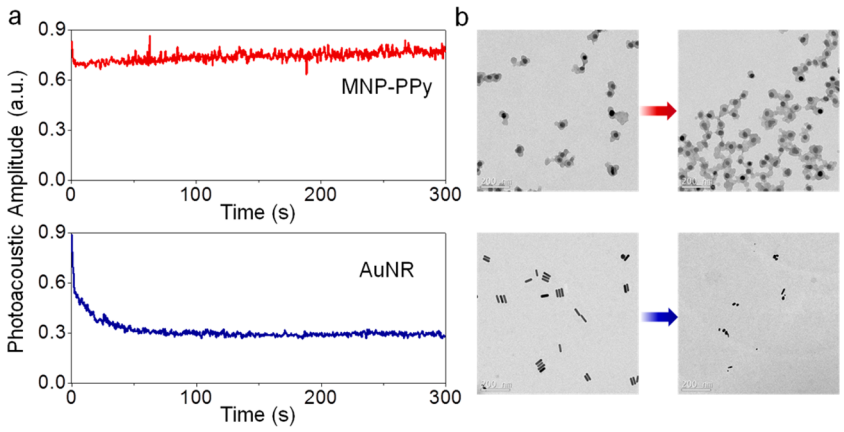

Figure 4. Photothermal stability of MNP−PPy hybrid nanoparticles compared with gold nanorods at the same mass (30 μg mL^{-1}) concentrations in poly(vinyl alcohol) (PVA) phantoms. (a) Photoacoustic amplitudes of indicated nanoparticles in phantoms versus laser exposure time. The photoacoustic signal amplitude generated by gold nanorods drops from 0.89 to 0.27 after a 300 s laser irradiation. (b) TEM images of typical MNP−PPy nanoparticles (top) and gold nanorods (bottom) before and after laser irradiation treatment for 300 s. A single laser pulse at 800 nm with a laser fluence of 11 mJ/cm^2 and a pulse repetition rate of 20 Hz was utilized for all experiments. The total pulse number for each sample is 6000 within 300 s. The fluence is calculated by divided the pulse energy by the illumination area.

designed. For example, if bulk Fe^{3+} is used as the oxidant, polymerization of PPy would occur in solution regardless of the presence of MNPs (Figure 3d). Using APS as the oxidant in the presence of SDS, in contrast, would slow formation of solid PPy nanoparticles (homogeneous nucleation) and their aggregates. At the same time, because the reaction is conducted in acidic conditions (pH = 2−3) where Fe ions are slowly released from MNP, PPy oxidation on the MNP surface by Fe^{3+} is promoted by the MNP surface (reduced Fe^{3+} can be regenerated by bulk APS). It is worth mentioning that the pH was optimized to 2−3 because more acidic conditions dissolve MNPs too fast, whereas higher pH dramatically reduces the polymerization rate (Figure S2, Supporting Information).

To address the issue of agent stability under the intense laser irradiation required for photoacoustic imaging, we directly compared the photostability of MNP−PPy and gold nanorod, one of the best photoacoustic contrast agents commonly used as a benchmark. At the same mass concentrations, the amplitudes of photoacoustic signals generated with MNP−PPy and gold nanorods are similar (Figure S3, Supporting Information). The photostability of MNP−PPy nanoparticles, however, is significantly better. As shown in Figure S4, Supporting Information, when the MNP−PPy nanoparticles and gold nanorods are treated with a low-intensity pulsed laser (5 mJ/cm^2, pulse repetition rate of 20 Hz), both MNP−PPy and gold nanorods remain intact during continuous illumination of 300 s, as indicated by the constant photoacoustic signals. When the laser intensity increases to 11 mJ/cm^2, however, the photoacoustic signal of gold nanorods drops approximately 40% within just 2 s of illumination and continuously decays over time (Figure 4a), because they quickly degrade and lose their characteristic NIR absorption. Under the same condition, the photoacoustic signal from MNP−PPy is still constant, revealing their superior photostability and suitability for long-term mmPA imaging. TEM imaging before and after laser irradiation confirmed these results. As shown in Figure 4b, the MNP−PPy nanoparticles are largely intact after exposure to laser irradiation, but the gold nanorods are shortened and fragmented.

The greatly improved photostability of PPy nanoparticles over gold nanorods is a little surprising since inorganic nanomaterials are generally perceived to be more photostable than organic compounds. For example, semiconductor quantum dots are thousands of times more stable than organic fluorophores.[33,34] However, gold nanorods are not the most thermodynamically stable structure and can melt or fragment into spherical particles. High-resolution TEM has revealed that, unlike thermal melting, which starts from the nanomaterial surface, photothermal melting of gold nanorods starts from defect formation inside the nanorods.[9] In contrast, the photostability of conjugated polymers can be optimized by varying their molecular structures, encapsulation matrix, and packaging.[35,36] This photostability comparison demonstrates MNP−PPy's outstanding potential for bioimaging utilizing high-intensity or extended laser illumination.

For cell labeling, the MNP−PPy nanoparticles are further pegylated and conjugated with FA as a model cell targeting ligand. HeLa cells are treated with the targeted MNP−PPy at a concentration of 0.5 nM for 2 h, in comparison with nontargeted MNP−PPy and MNP−PPy−PEG. Using Prussian blue staining (formation of ferricyanide), nanoparticle uptake can be directly visualized and qualitatively analyzed. Figure 5 shows pronounced differences between the targeted nanoparticles (Figure 5e) and the control groups (no treatment, treatment with MNP−PPy nanoparticles, or

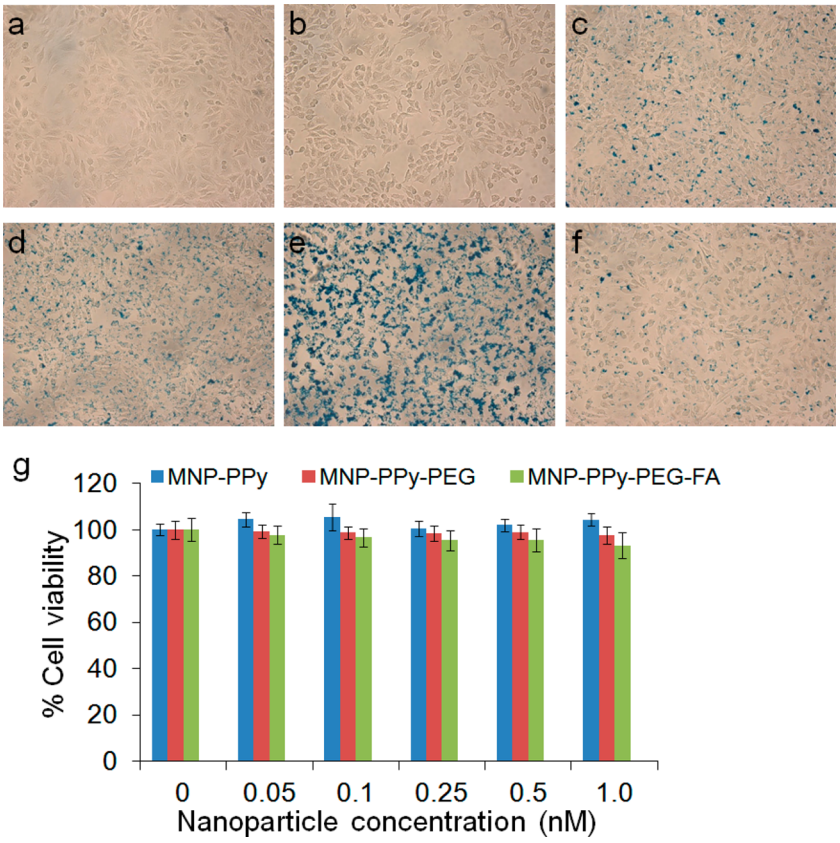

Figure 5. Targeting specificity and cytotoxicity of hybrid nanoparticles. Bright field micrographs of HeLa cells (a) with no treatment and treated with (b) Prussian blue, (c) 0.5 nM MNP−PPy nanoparticles, (d) MNP−PPy−PEG nanoparticles, (e) MNP−PPy−PEG−FA nanoparticles, and (f) MNP−PPy−PEG−FA nanoparticles together with 1 mM free FA. (c−f) Stained with Prussian blue. (g) Dose-dependent cytotoxicity of MNP−PPy, MNP−PPy−PEG, and MNP−PPy−PEG−FA nanoparticles in HeLa cells plotted against the control groups with no treatment. In the concentration range probed between 0 and 1.0 nM, the three types of nanoparticles do not show significant cytotoxicity. Error bars represent standard deviations of three separate measurements.

MNP−PPy−PEG nanoparticles, Figure 5a−d). To further confirm that targeting was achieved through FA targeting ligands, a competition assay was conducted by coincubation of the targeted nanoparticles with free folic acid molecules. As shown in Figure 5f, Prussian blue staining is reduced to approximately the same level of the pegylated nanoparticles (Figure 5d), demonstrating targeting specificity.

Before moving to tumor cell detection with mmPA, a remaining characterization experiment for the MNP−PPy hybrid nanoparticles examines cytotoxicity. As shown in Figure 5g, cell viability is not affected by the final FA-targeted MNP−PPy or the control particles (original unmodified MNP−PPy and pegylated MNP−PPy) in the concentration range from 0 to 1.0 nM. At 1.0 nM, twice as high as the particle concentration used in cell labeling, cell viability only decreases by 7% for the FA-targeted MNP−PPy, which has the highest cell uptake.

Next, we evaluated the design and performance of the new generation of mmPA technology featuring two major innovations for *in vivo* applications. Figure 1b demonstrates the concept of the first innovation, multicycle magnetomotion. Under simplified imaging conditions where specific signals from contrast agents are buried by static background signals, single-cycle magnetic-induced physical movements of the contrast agent (or cells labeled with the contrast agents) is sufficient to retrieve the moving signal from the contrast agent and completely reject the background static signals (1st generation mmPA). For *in vivo* imaging, however, the motion sources can be complex, including magnetic motion as well as physiological movements such as cardiac and respiratory motions (background motions). To mitigate the interference from background motions, previous *in vivo* studies have taken advantage of the "grace period" of breathing cycles using single element scanning to form a 2D image.[12] Hence, continuous measurements cannot be performed since each sequence has to be triggered on every breathing cycle, limiting the frame rate to less than 1 line/s.

In addition, thresholding of displacement magnitudes also has major limitations,[2,12] because the amplitudes of background motion vary dramatically and a consistent threshold is difficult to find. For second generation mmPA, we acquire 2-D (3-D) photoacoustic images in a single laser shot using a conventional

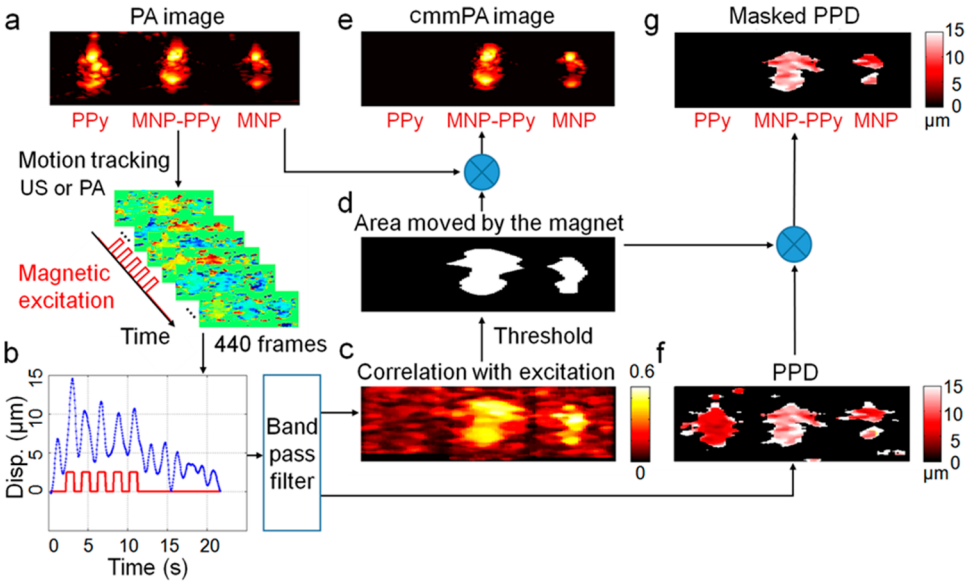

Figure 6. Data processing of cyclic mmPA. A PVA phantom with three 2 mm diameter inclusions, in which the one on the left contains PPy nanoparticles with absorption comparable to 5 nM MNP−PPy hybrid nanoparticles placed in the center of phantom, and the third inclusion on the right contains 5 nM MNPs. (a) A conventional photoacoustic image of this phantom presented on a logarithmic scale over a 40 dB display range. (b) A representative displacement of MNP−PPy inclusion during 5-cycle square wave magnetic excitation with a frequency of 0.5 Hz. (c) Correlation with excitation map (CEM) utilized to produce photoacoustic image background suppression with a threshold of 0.5. (d) Mask produced by thresholding the CEM with 0.5 and used to identify MNPs. (e) The cmmPA images produced by multiplying the threshold mask from (a), in which the PPy inclusion is almost completely suppressed. (f) Peak to peak displacement images before and (g) after background suppression with the threshold mask.

1-D (2-D) ultrasound array and a cyclic excitation method (thus dubbed cmmPA) to separate magnetomotive displacements from background motions. As a result, the threshold is independent of displacement amplitude and only depends on the time coherence of the displacements. Thus, both the amplitude and phase of displacements are taken into account. This cmmPA technology enables real-time mmPA *in vivo* even with significant physiological motions. Magnetically induced displacements with frequency ranging from 1 to 50 Hz and velocities up to 1 cm/s can be used to resolve molecular events with enhanced time resolution.

To evaluate cmmPA, three cylindrical inclusions, PPy, MNP−PPy, and MNP, were embedded in a poly(vinyl alcohol) (PVA) phantom. PPy NPs with absorption comparable to 5 nM MNP−PPy nanoparticles serve as the negative control for magnetic displacement, and MNPs (5 nM) serve as the negative control for NIR absorbance. An electromagnet (0.7 T at the source and approximately 0.2 T at the inclusion region) outputs pulsed magnetic fields with tunable frequencies. Figure 6a shows the cross-sectional photoacoustic image on a dB scale. Illuminated with a pulsed laser at 800 nm, the MNP−PPy and PPy inclusions show similar photoacoustic signal intensity, whereas the photoacoustic signal of the MNP inclusion is approximately 1 order of magnitude lower because of the low absorbance of MNP in the NIR spectrum.

A series of photoacoustic images (440 frames over 22 s) were recorded during which 5 cycles of 0.5 Hz magnetic movements were applied (Figure 6b). The photoacoustic images were beamformed using a simple delay-and-sum approach, and the resultant analytical signals were filtered with a bandpass filter ([0.35−1.83 Hz]) in the time direction. The motion of every pixel in the photoacoustic image is tracked using a speckle tracking algorithm,[37,38] and the corresponding displacement curve is cross-correlated with a bipolar derivative of the magnetic shaking signal (Figure 6c). This correlation with excitation map is referred to as CEM. By setting a threshold on the CEM (0.5 in the current study), an image mask (Figure 6d) can be created to reject both stationary signals and displacements that are not synchronized with magnetic shaking, such as slow physiological motion or drifts and high-frequency vibration artifacts. Indeed, when this mask is applied to the original photoacoustic image with the three inclusions, signals from MNP−PPy and MNP are retained whereas those from PPy are filtered out (Figure 6e).

Figure 6g presents the peak-to-peak displacement (PPD) map (Figure 6f) after applying the cmmPA mask over it. This PPD map can be useful for further quantitative analysis. For example, *in vivo* tumor targeting could result in increasing PPD over time at the lesion site after injection as nanoparticles accumulate. Alternatively, the quality of motion estimates can also be used as an additional mask to eliminate poor signal regions which can be affected by artifacts from bright neighboring regions, resulting in high values in CEM.

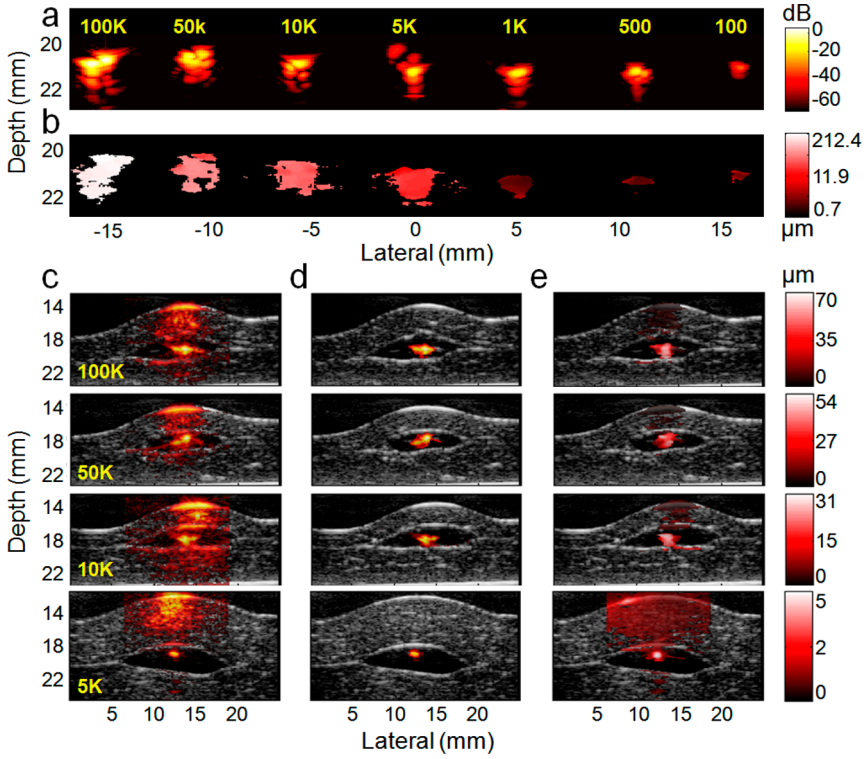

Figure 7. Sensitivity and selectivity of cmmPA imaging for cancer cell detection through photoacoustic speckle tracking (PAST, 0.5 Hz magnetic excitation). (a) Photoacoustic images of the phantom embedded with seven cell pellets (cell number from 100 to 100k) on a logarithmic scale over a 70 dB display range. (b) Peak to peak displacement image over a display range of 0.7−212.4 μm. Magnetic displacement decreases with smaller tumor size. (c−e) *Ex vivo* photoacoustic and cmmPA images of cell pellets (cell number from 5k to 100k) embedded in the middle of two porcine liver slices (producing strong background signals). (c) Photoacoustic and (d) cmmPA images though PAST (hot colors) superimposed on ultrasound images (gray colors) on a logarithmic scale over a normalized dB display range. The black region around the center hot spot (cell pellet) corresponds to the thin acoustically and optically transparent PVA layer used to encapsulate the cell pellets to avoid cell diffusion in tissues. (e) Displacement images of cell pellets over various displacement ranges.

We define the quality of speckle tracking as the mean value over all the frames of the normalized interframe cross-correlation magnitude. If corresponding regions in two consecutive images are too different (low signal-to-noise ratio or artifact), the quality coefficients of these regions are typically lower than those of bright regions. By setting a second threshold on the map of quality coefficient, poor signal regions can be filtered out.

To test cmmPA for tumor cell imaging, we first evaluated photoacoustic sensitivity under background-free conditions and the minimum number of cells required to detect magnetically induced motion. HeLa cells tagged with the targeted MNP−PPy nanoparticles are pelleted, mimicking solid tumors, and embedded in a PVA phantom with elasticity similar to that of biological tissues (Young's modulus $E = 4-8$ kPa). As shown in Figure 7a, because the PVA phantom has low NIR light absorbance and, consequently, low photoacoustic signals, all seven cell pellets containing 100 to 100 000 tumor cells are clearly visible.

For magneto displacement characterization, peak-to-peak displacement was mapped for the seven cell pellets, using photoacoustic motion tracking. Figure 7b shows that tumor displacements vary from approximately 2 to 200 μm, depending on the total number of magnetic nanoparticles in the embedded cells, which contributes to the final magnetic response. Despite the general trend that larger tumor cell clusters move more than smaller ones, no simple relationship between displacements and cell numbers is found, because the volume of each inclusion cannot be controlled easily by manual pipetting of cells. Still, the magnetic motion of 100 tagged cells can be clearly differentiated using the cmmPA technology. These studies show that a small number of cells tagged with photoacoustic contrast agents can be readily detected under background free conditions.

In the presence of biological tissues, however, signals from the small number of cells are difficult to distinguish from tissue background signals. We evaluated cyclic mmPA's ability to enhance image contrast. MNP−PPy tagged tumor cell pellets were embedded in a PVA phantom and sandwiched between two slices of porcine liver tissue. Pellets of 100k, 50k, 10k, and 5k cells are used in this study because they are simple models of solid tumors and are clearly visible when cutting the PVA phantom around them (a smaller number of cells are hard to visualize during phantom cutting). Photoacoustic tracking (magnet excitation at 0.5 Hz) was used for cmmPA.

Figure 7c shows photoacoustic images (hot color scale) superimposed on ultrasound images (gray scale, to show tissue structure). The black region around the central hot spot (tumor cells) corresponds to the acoustically and optically transparent PVA layer. Clearly, due to the high photoacoustic background of liver tissue, tumor cells cannot be distinguished without *a priori* information on their location. Quantitative measurements show that the contrasts on dB-scale images of the four inclusions are +3.9, +0.83, −6.07, and −0.25 dB, respectively, suggesting that small tumors cannot be detected by conventional photoacoustic imaging. In contrast, cmmPA images (Figure 7d) show clear isolated signals from the tumor cells with the background almost completely suppressed. The contrast improves by +31.3, +34.5, +41.4, and +29.1 dB, approximately 2 orders of magnitude better than the original photoacoustic images.

On the baiss of these remarkable results, we expect that a smaller number of cells in the 100s to 1000s range can be detected with this technology, especially using MNPs of higher magnetic permeability, stronger magnets, and additional repetition cycles of magnetic shaking. Considering current tumors are often detected when they reach mm^3 and cm^3 in size, which constitutes 10^6 and 10^9 tumor cells,[39] mmPA shows an excellent potential for early diagnosis of small lesions. In addition, quantitative magnetic displacement values can potentially provide information correlated with the concentration of cells per imaging pixel (voxel). This hypothesis will be tested in future studies.

For *in vivo* testing, the frequencies of physiologic motions should be considered for cmmPA imaging. For example, human cardiac and respiration frequency are 0.6−1.2 and 0.1−0.5 Hz, respectively, which are 5−10 times lower than those of mice. Clearly, the frequency of magnetic motions (0.5 Hz) overlaps with (or is too close to) physiological motion frequencies, making the background motion artifact difficult to reject. Therefore, the magnetic oscillation should be increased to a higher frequency. Note that the increased frequency leads to reduced displacement during each magnetic pulse; thus, the frequency and displacement should be balanced for both sensitive and specific detection of magnetic motions (e.g., 10 or 20 Hz). A practical difficulty encountered by first generation mmPA, however, is the slow frame rate of photoacoustic speckle tracking (PAST), limited by the laser repetition rate (in our current setup, 20 Hz pulsed laser). Reliable speckle tracking (image patterns are tracked consecutively frame to frame) requires a large number of images to be captured during each magnetic pulse, but the frame rate of PAST is too slow when magnetic excitation is at 10 or 20 Hz. This issue is addressed by another key innovation in second-generation mmPA, hybridizing photoacoustic imaging with USST, because US plane wave imaging enables kHz frame rates.

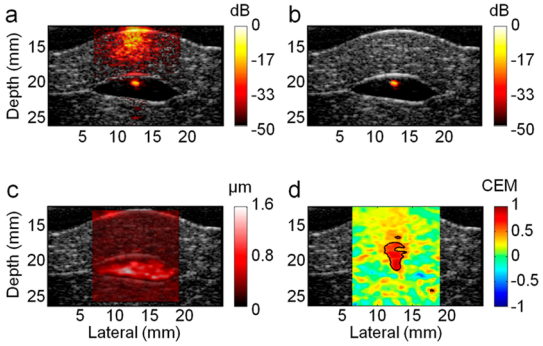

Figure 8. Sensitivity and selectivity of *ex vivo* cmmPA imaging using US speckle tracking (USST). (a) Photoacoustic image of the cell pellet containing 5k cancer cells overlaid on ultrasound images (gray colors) on a logarithmic scale over a 50 dB display range. (b) cmmPA image obtained with USST (10 Hz magnetic excitation). (c) Peak to peak displacement image over a display range of 0−1.6 μm. (d) Correlation with an excitation map utilized to produce photoacoustic image background suppression with a threshold of 0.5.

To evaluate US tracking performance, the inclusion of 5k tumor cells, which is the detection limit of PAST at a magnet excitation of 0.5 Hz, was probed again using USST (magnet excitation at 10 Hz). Figure 8b shows clear isolated cell signals after background suppression from the photoacoustic image (Figure 8a). The contrast improves by +30.9 dB from +7.3 dB, consistent with the order of PAST improvement (+29.1 dB). However, it is important to note the difference between the results obtained with USST and PAST. Using PAST at the magnetic excitation of 0.5 Hz, the peak displacement is on the order of 5 μm. At magnet excitation 20 times faster, USST readily detects PPD at the 1 μm level (Figure 8c). Remarkably, as shown in Figure 8d, the correlation map has high contrast with a clear delineation. It confirms that, regardless of the speckle checking method, thresholding based on correlation functions is much more robust than thresholding on displacement magnitude in the presence of significant physiological motion.

This technique was evaluated *in vivo* using a mouse model bearing subcutaneous injected HeLa cells pretagged with MNP−PPy nanoparticles. All animal procedures were approved by the University of Washington Institutional Animal Care and Use Committee. The instrument setup is shown in Figure 9a,b. An imaging array working at 15 MHz (element pitch = 0.1 mm) was connected to an ultrasound scanner. Light was delivered by two optical fibers, and a magnetic core was positioned near the targeted zone. A translation stage was used to scan all devices along the mouse body for full 3-D data acquisition. Mice were anesthetized with isoflurane and positioned on an angled bench placed inside a tank. 10k tagged cells mixed with 100 μL of Pluronic-127 gel (30%), a thermoresponsive and biodegradable polymer to hold the cells underneath the skin, were injected subcutaneously into the dorsum. An 8-cycle, 20 Hz magnetic excitation

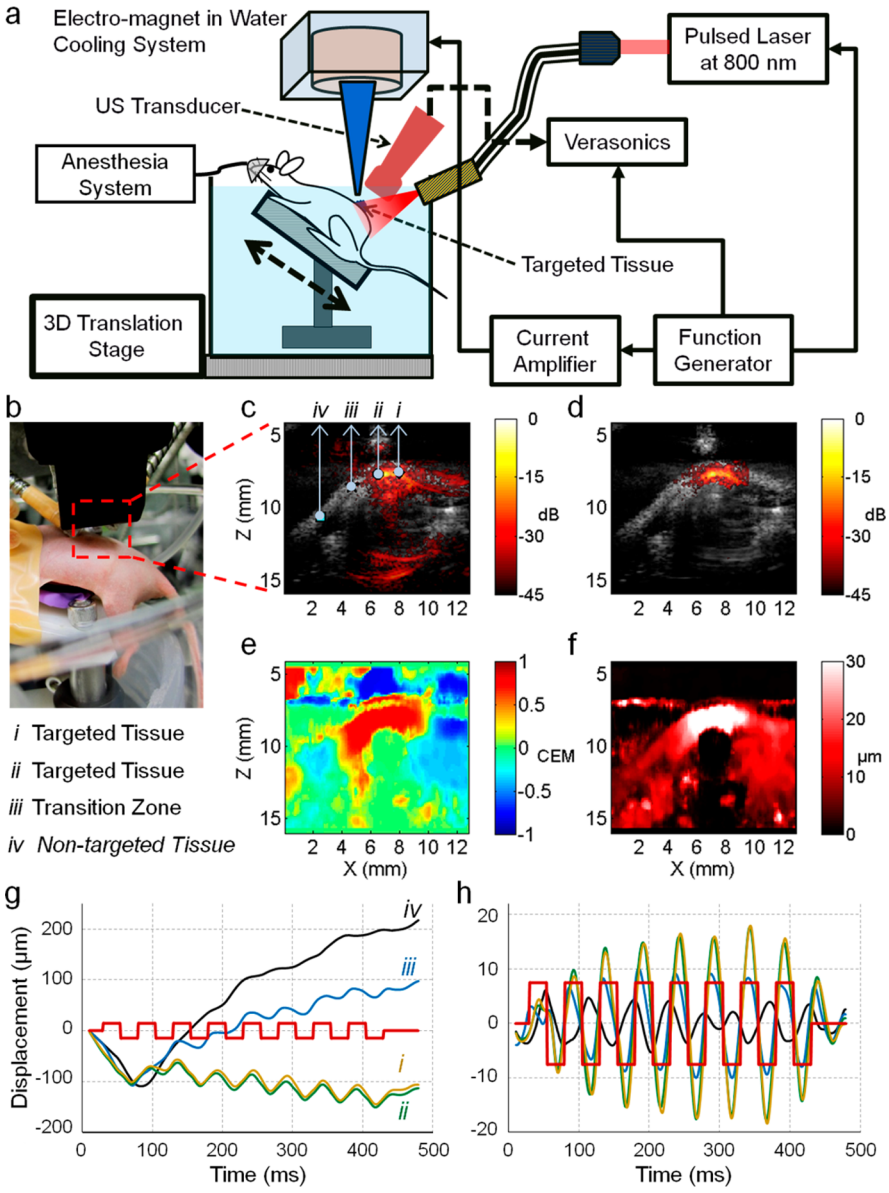

Figure 9. *In vivo* **cmmPA imaging of cancer cells from a mouse model following subcutaneously injection. (a) Schematic of the *in vivo* cmmPA imaging setup. (b) Photograph of a mouse imaging experiment. Anesthetized mouse positioned on an angled bench placed inside a tank and subcutaneously injected 10k cancer cells (tagged with nanoparticles) into the dorsum site, which was imaged (after 1 h injection) through conventional photoacoustic imaging, cmmPA and US. (c) Photoacoustic/ultrasound overlaid image of tumor region containing (i, ii) targeted, (iii) transition, and (iv) nontargeted zones in the dorsum of living mice. (d) cmmPA image obtained with USST using 8-cycle 20 Hz magnetic excitation. (e) Correlation with excitation map utilized to produce photoacoustic image background suppression with a threshold of 0.5. (f) Peak to peak displacement image over a display range of 0−30 μm. (g) Raw cumulative displacements at zones indicated by markers (i−iv) on the photoacoustic image (c). (h) Filtered displacement curves using a bandpass filter [8−70] Hz. The red square wave indicates magnetic excitation cycles.**

was applied during acquisition of 400 US frames (total imaging time of 0.5 s, frame rate of 800 Hz).

Figure 9c presents a photoacoustic image (hot scale) overlaid on a US image. The injected cells cannot be distinguished from background tissues. However, the cmmPA image (Figure 9d) shows a clearly delineated area corresponding to the tagged cells lying beneath the skin. This masking was obtained using a threshold of 0.5 on the correlation with excitation map (Figure 9e) and a second threshold of 0.9 on the quality coefficient of motion tracking. Even if the peak-to-peak displacement map (Figure 9f) could be used to obtain similar information, the amplitude of the threshold would have to be set to different values depending on the conditions without a universal standard. Moreover, a region with high displacements can be identified along a thin horizontal line at a depth of 7 mm through the PPD map, while corresponding to image artifacts moving incoherently with the magnet, which is negative in CEM (Figure 9e).

Figure 9g presents the absolute displacement curves at different locations (marked from i to iv with

arrows pointing to them in Figure 9c). It can be seen that physiological motion produces a lower frequency response with continuous large drifting displacement than that from the magnet. These motions can be low-pass filtered, and the resulting signals are shown in Figure 9h. Coherent motion is retrieved for the points i and ii at the center of the targeted zone whereas an out-of-phase smaller motion is obtained a few millimeters away (point iii), corresponding to the propagation of a shear/surface mechanical wave along the skin. Low-frequency mechanical waves (surface or shear waves) can possibly propagate away from the targeted area and create a wrong interpretation about the measured displacements in terms of source delineation. The bandpass filtering can also result in ringing of wideband physiological motion. Thus, it is essential to account for the phase of the displacement to retrieve the location of the source of magnetic displacements.

The ultimate limit of induced displacements for the magnetic modulation technique is determined by the frequency (f) of the ultrasound signal and the electronic signal-to-noise ratio (SNR) of the imaging system. A simple propagation of error analysis yields the minimum detector displacement as a function of these two parameters:

$$\text{displacement}_{\text{min}} = \left[\frac{c}{4\pi \text{SNR}}\right]\left[\frac{1}{f}\right]$$

where c is the sound speed, f is the frequency, and the SNR is a dimensionless number. For a 15 MHz transducer and an SNR of 100 (40 dB, a typical value for the ultrasound images used in this study), this represents a minimum detectable displacement of 8 μm. Because a correlation technique is used over several periods of the magnetic excitation, representing a dwell interval on the order of 100 ultrasound frames, this means the minimum detectable displacement for the modulation technique should be on the order of 0.8 μm (i.e., $1/(100)^{1/2}$ times 8 μm). As is evident from the results presented in Figure 8, submicrometer displacements are clearly detected and can be used to produce a robust correlation with excitation map (CEM), leading to a highly selective cmmPA image.

The overall robustness of the magnetic modulation technique is a combination of its inherent sensitivity and immunity to background motion. Clearly, the displacement sensitivity approaches theoretical limits, as noted above. The results presented in Figure 9 show that cmmPA can produce highly selective imaging of cancer cells tagged with magnetic nanoparticles for background displacements well over an order of magnitude larger than magnetically induced ones. Clearly, there will be cases where background motion may be several orders of magnitude larger than magnetically induced motion, especially as the frequency of the magnetic excitation is increased, but simple time gating can be used to reduce this ratio to manageable levels. Consequently, the magnetic modulation technique presented here has both the sensitivity and robustness for potential *in vivo* application.

CONCLUSIONS

In summary, we have developed magneto-optical dual functional particles that are compact and uniform in size, NIR light absorbing, and scalable in synthesis. Compared to the conventional gold nanostructure-based NIR absorbers, the MNP−PPy nanoparticles are significantly more stable against laser irradiation, which is critical for imaging applications involving high-intensity lasers. In parallel, we have also developed a new generation of mmPA technology featuring two key innovations in motion detection, time coherence of displacement with cyclic magnetic excitation and ultrasound-based speckle tracking. In contrast to the first generation mmPA based on the absolute amplitude of magnetic-induced motion, the new system is capable of distinguishing contrast agent movement from physiological motions. Combined, the new imaging probe and cmmPA technology enable the demonstration of mmPA in live animals, a key step toward ultrasensitive molecular imaging and clinical translation.

EXPERIMENTAL SECTION

Chemicals. Unless specified, chemicals were purchased from Sigma-Aldrich and used without further purification. Iron oxide MNPs (SHP-40) and a Prussian Blue staining kit were purchased from Oceannanotech LLC. FA−PEG−NH_2 (MW 3400) and PEG−NH_2 (MW 5000) were purchased from NANOCS. The CellTiter-Blue viability assay was purchased from Promega. Ultrapure water was obtained from a Milli-Q water purifier.

PPy Nanoshell Growth. Water-soluble MNPs (70 nM, 60 μL) and SDS (120 mM, 300 μL) were mixed in 4.5 mL of DI water, followed by adjusting the pH of the solution to 2−3 through slow addition of HCl (1 N). Different pH values were adjusted for the control experiments. After approximately a 10 min incubation, Py (20 mM, 400 μL) and Py−COOH (20 mM, 50 μL) were added into the MNP solution. For homopolymerization, 450 μL of Py (20 mM) was added without Py−COOH. After brief vortexing, the oxidant $(NH_4)_2S_2O_8$ (2 mM, 4.5 mL) was added to the solution to promote Py polymerization. The reaction mixture was kept at room temperature with stirring for 10 h. The as synthesized MNP−PPy core−shell nanoparticles were purified with repeated centrifugation (12 000g for 15 min 3×) and magnetic separation (2×). The purified MNP−PPy NPs were redispersed in 2.8 mL of DI water.

Conjugation with PEG and FA. PEG−NH_2 or FA−PEG−NH_2 was linked to the MNP−PPy particles using 1-ethyl-3-[3-(dimethylamino)propyl] carbodiimide (EDAC) as the cross-linker. PEG−NH_2 (1 mg) or FA−PEG−NH_2 (1 mg) was first dissolved in 100 μL of dimethyl sulfoxide (DMSO), followed by adding 2.8 mL above the MNP−PPy NP solution. After vortexing for 10 min, EDAC (2 mg/mL) dissolved in 100 μL of DMSO was quickly added into the NP solution. The reaction mixture was

incubated at room temperature for 6−8 h in the dark with continuous mixing. The final particles were purified by magnetic separation (3×).

Cell Viability. The CellTiter-Blue cell viability assay was utilized to test the cytotoxicity of the nanoparticles in living cells. After seeding HeLa in a 96-well plate with 180 μL of cell culture medium for 24 h, different kinds of nanoprobes (20 μL) with various molar concentrations (0, 0.5, 1, 2.5, 5, and 10 nM) were added to 180 μL of cell culture medium in each well and incubated for 24 h in the dark. The cells were washed three times by 1× phosphate buffered saline (PBS) buffer, followed by addition of the dye solution (20 μL) and cell culture medium (80 μL) to each well and incubation for 4 h in the dark. Fluorescence at $560_{Ex}/590_{EM}$ was recorded using a 96-well plate reader (Tecan Infinite M200).

Cell Preparation for mmPA. HeLa cells expressing folate receptor were grown to 80% confluence and incubated with the folic acid targeted hybrid nanoprobes or control nanoparticles (0.5 nM) in 10 mL of PBS buffer for 2 h. After removing unbound particles through three times of a PBS buffer wash, the cells were trypsinized, washed three times again by centrifugation (1000 rpm, 5 min), fixed in 4% formalin for 30 min, counted on a hemocytometer, and stored at 4 °C.

Nanoparticle and Targeted Cell Embedded Phantom Preparation. A 3 mm thick disk phantom of 10% (weight percentage) poly(vinyl alcohol) (PVA) was constructed using one short freeze−thaw (10 min) cycle. Three 2 mm-diameter cylindrical inclusions (1 cm length) made of 10% PVA mixed with 8% (weight percentage) 15 μm polystyrene beads and 10 nM different nanoprobes (PPy, MNP−PPy, and MNP) were placed parallel within the 3 mm thick PVA phantom. After a 10 min freeze−thaw cycle, another 3 mm thick PVA disk was placed on the top to encapsulate the whole phantom, followed by 2 freeze−thaw (20 min) cycles. For the cell embedded phantom, instead of cylindrical inclusions, nanoparticle tagged cancer cells (100, 500, 1K, 5k, 10k, 50k, and 100k) were trapped at the end of pipet tips by magnets and transferred into the PVA phantom. The freeze−thaw methods are the same as above.

Targeted Cell Embedded Porcine Liver Tissue Preparation. The nanoparticle tagged cancer cells (5k, 10k, 50k, and 100k) were trapped at the end of pipet tips by magnets and embedded in the 10% PVA phantom. One hundred and twenty-five mm^3 phantoms with cells inside were extracted with a knife and then embedded between 2 slices of 8 mm porcine liver tissue to mimic a tissue background. Note that cells were not directly spread onto the liver slices to avoid cell diffusion.

CmmPA Magnet System. A soft iron core has been machined to form a cone with a flat end tip of 2 mm diameter and a large diameter of 26 mm. This core was placed within a solenoid encapsulated in an aluminum housing (Ledex, USA). The surface of the electromagnet was coated with nonabrasive silicon and encapsulated in a water-cooled aluminum box to avoid virtual displacements due to the thermally induced changes in sound speed within the sample. The electromagnet was excited with a linear current amplifier module (Quanser, Canada) driven by a function generator, producing cyclic 0.7 T pulses at its surface and a 50 mT/mm gradient in the axial direction, 3 mm away from the surface. In this study, excitations composed of 5 cycles of a square wave (low: 0 V; high: +V) have been used for photoacoustic speckle tracking (PAST). The frequency of the square wave was set to 0.5 Hz to allow a sufficient number of photoacoustic images to be captured with a laser repetition rate limited to 20 Hz. For US speckle tracking (USST), 10 or 20 Hz or higher frequency magnetic excitation was utilized to record a sufficient number of both photoacoustic images captured with a laser repetition rate limited to 20 Hz and US images captured with a frame rate of 800 Hz.

***In Vitro* Cyclic mmPA Imaging Setup.** The electromagnet was placed under a water tank holding the phantom with a minimum distance to the region of interest of 3 mm. A frequency-doubled YAG pulsed laser with 5 ns pulse width pumped an optical parametric oscillator to illuminate the PVA phantom at 800 nm wavelength with a flunece of 14 mJ/cm^2. A linear ultrasound array (AT8L12-5_50 mm, Broadsound, Taiwan) connected to a programmable ultrasound scanner (Verasonics, Seattle, USA) acquired RF signals in a single image acquisition of 440 frames at the repetition rate of the laser (20 Hz). The magnet system was first adjusted relative to the US probe. While moving the sample in one direction, the cells were first identified with real time photoacoustic imaging. The ultrasound array was precisely positioned by maximizing the photoacoustic signal amplitude, enabling positioning of the tagged cells under the magnet at a distance of 5−6 mm. The mmPA imaging sequence was then executed. At the beginning of the imaging sequence, the ultrasound scanner triggers the function generator driving the magnetic excitation. Online displacement calculation and filtering implemented in Matlab can provide a final mmPA image within a few seconds.

***In Vivo* Cyclic mmPA Imaging.** The *in vivo* setup was modified from the *in vitro* cmmPA one. An imaging array working at 15 MHz (element pitch = 0.1 mm, Vermon, France) with a compact housing was connected to a Verasonics Vantage ultrasound scanner. The laser was delivered by two optical fibers, and the magnetic core was placed with all elements closer to each other, facing the tumor sites. A stage was used to scan all devices along the mouse body for full 3-D data acquisition. *In vivo* cmmPA imaging was evaluated on mice (female, U.S.A.). The animal study protocol was approved by the Institutional Animal Care and Use Committee at University of Washington. Mice were positioned on an angled bench placed inside a tank filled with 36 °C water. 10k nanoparticle tagged cancer cells were suspended into 30% Pluronic-127 (PF127) solution and subcutaneously injected into the dorsum of mice to form a thermogel. A total of 100 μL of the cancer cells/PF127 mixture was subcutaneously injected into the dorsum of mice after anesthesia with isoflurane. Eight cycles of 20 Hz magnetic excitations were applied during acquisition of 400 US frames (total imaging time of 0.5 s, frame rate of 800 Hz). Mice were euthanized via CO_2 asphyxiation at the end of the experiments.

Conflict of Interest: The authors declare no competing financial interest.

Acknowledgment. This work was supported in part by NIH (R01 CA170734, U19 ES019545, and R01 EB016034), the Washington Life Sciences Discovery Fund (3292512), and the Department of Bioengineering at the University of Washington. We are grateful to Prof. Mingyuan Gao at the Chinese Academy of Sciences, Prof. Terrance Kavanagh at UW DOEHS, and Dr. Pavel Zrazhevskiy at University of Washington for fruitful discussions on nanotoxicity and hybrid nanoparticle synthesis. We are also grateful to Jeff Magula for manufacturing the electromagnet.

Supporting Information Available: Nanoparticle absorption and photostability characterized with photoacoustic imaging, pH effect on polypyrrole coating, particle stability in oscillating magnetic fields, and a detailed procedure of photoacoustic-based measurement of absorption spectra. This material is available free of charge *via* the Internet at http://pubs.acs.org.

REFERENCES AND NOTES

1. Siegel, R.; Ma, J.; Zou, Z.; Jemal, A. Cancer Statistics. *Ca-Cancer J. Clin.* **2014**, *64*, 9–29.
2. Jin, Y. D.; Jia, C. X.; Huang, S. W.; O'Donnell, M.; Gao, X. H. Multifunctional Nanoparticles as Coupled Contrast Agents. *Nat. Commun.* **2010**, *1*, 41.
3. Galanzha, E. I.; Shashkov, E. V.; Kelly, T.; Kim, J. W.; Yang, L. L.; Zharov, V. P. *In Vivo* Magnetic Enrichment and Multiplex Photoacoustic Detection of Circulating Tumour cells. *Nat. Nanotechnol.* **2009**, *4*, 855–860.
4. Li, J. W.; Liu, J.; Wei, C. W.; Liu, B.; O'Donnell, M.; Gao, X. H. Emerging Applications of Conjugated Polymers in Molecular Imaging. *Phys. Chem. Chem. Phys.* **2013**, *15*, 17006–17015.
5. Pu, K. Y.; Shuhendler, A. J.; Jokerst, J. V.; Mei, J. G.; Gambhir, S. S.; Bao, Z. N.; Rao, J. H. Semiconducting Polymer Nanoparticles as Photoacoustic Molecular Imaging Probes in Living Mice. *Nat. Nanotechnol.* **2014**, *9*, 233–239.
6. Wang, L. H. V.; Hu, S. Photoacoustic Tomography: *In Vivo* Imaging From Organelles to Organs. *Science* **2012**, *335*, 1458–1462.

7. Link, S.; Burda, C.; Mohamed, M. B.; Nikoobakht, B.; El-Sayed, M. A. Laser Photothermal Melting and Fragmentation of Gold Nanorods: Energy and Laser Pulse-Width Dependence. *J. Phys. Chem. A* **1999**, *103*, 1165–1170.
8. Link, S.; Burda, C.; Nikoobakht, B.; El-Sayed, M. A. Laser-Induced Shape Changes of Colloidal Gold Nanorods Using Femtosecond and Nanosecond Laser Pulses. *J. Phys. Chem. B* **2000**, *104*, 6152–6163.
9. Link, S.; Wang, Z. L.; El-Sayed, M. A. How Does a Gold Nanorod Melt? *J. Phys. Chem. B* **2000**, *104*, 7867–7870.
10. Hu, X.; Gao, X. Multilayer Coating of Gold Nanorods for Combined Stability and Biocompatibility. *Phys. Chem. Chem. Phys.* **2011**, *13*, 10028–10035.
11. Chen, Y.-S.; Frey, W.; Kim, S.; Homan, K.; Kruizinga, P.; Sokolov, K.; Emelianov, S. Enhanced Thermal Stability of Silica-Coated Gold Nanorods for Photoacoustic Imaging and Image-Guided Therapy. *Opt. Exp.* **2010**, *18*, 8867–8878.
12. Mohammad, M.; Min, Q.; Li, L. M.; Dwight, K. R.; Keith, P. J.; Konstantin, V. S.; Stanislav, Y. E. Pulsed Magneto-Motive Ultrasound Imaging to Detect Intracellular Accumulation of Magnetic Nanoparticles. *Nanotechnology* **2010**, *22*, 415105.
13. Chun-Ling, Z.; Shang-Wei, C.; Shih-Fong, H.; Wei-Neng, L.; Chia-Chun, C. Synthesis of Core/Shell Metal Oxide/Polyaniline Nanocomposites and Hollow Polyaniline Capsules. *Nanotechnology* **2007**, *18*, 275604.
14. Lu, X.; Mao, H.; Zhang, W. Fabrication of Core-Shell Fe_3O_4/Polypyrrole and Hollow Polypyrrole Microspheres. *Polym. Compos.* **2009**, *30*, 847–854.
15. Jiang, W.; Kim, B. Y. S.; Rutka, J. T.; Chan, W. C. W. Nanoparticle-Mediated Cellular Response is Size-Dependent. *Nat. Nanotechnol.* **2008**, *3*, 145–150.
16. Cabral, H.; Matsumoto, Y.; Mizuno, K.; Chen, Q.; Murakami, M.; Kimura, M.; Terada, Y.; Kano, M. R.; Miyazono, K.; Uesaka, M.; Nishiyama, N.; Kataoka, K. Accumulation of Sub-100 nm Polymeric Micelles in Poorly Permeable Tumours Depends on Size. *Nat. Nanotechol.* **2011**, *6*, 815–823.
17. Wang, C.; Xu, H.; Liang, C.; Liu, Y.; Li, Z.; Yang, G.; Cheng, L.; Li, Y.; Liu, Z. Iron Oxide @ Polypyrrole Nanoparticles as a Multifunctional Drug Carrier for Remotely Controlled Cancer Therapy with Synergistic Antitumor Effect. *ACS Nano* **2013**, *7*, 6782–6795.
18. Ashis, D.; Amitabha, D.; De, S. K. Electrical Transport and Dielectric Relaxation in Fe_3O_4-Polypyrrole Hybrid Nanocomposites. *J. Phys.: Condens. Matter* **2005**, *17*, 5895.
19. Brezoi, D.-V.; Ion, R.-M. Phase Evolution Induced by Polypyrrole in Iron Oxide-Polypyrrole Nanocomposite. *Sens. Actuators, B: Chem.* **2005**, *109*, 171–175.
20. Chen, A.; Wang, H.; Zhao, B.; Li, X. The Preparation of Polypyrrole-Fe_3O_4 Nanocomposites by the Use of Common Ion Effect. *Synth. Met.* **2003**, *139*, 411–415.
21. Deng, J.; Peng, Y.; He, C.; Long, X.; Li, P.; Chan, A. S. C. Magnetic and Conducting Fe_3O_4—Polypyrrole Nanoparticles with Core-Shell Structure. *Polym. Int.* **2003**, *52*, 1182–1187.
22. Guo, Z.; Shin, K.; Karki, A.; Young, D.; Kaner, R.; Hahn, H. T. Fabrication and Characterization of Iron Oxide Nanoparticles Filled Polypyrrole Nanocomposites. *J. Nano. Res.* **2009**, *11*, 1441–1452.
23. Li, Y.; Yi, R.; Yan, A.; Deng, L.; Zhou, K.; Liu, X. Facile Synthesis and Properties of $ZnFe_2O_4$ and $ZnFe_2O_4$/Polypyrrole Core-Shell Nanoparticles. *Solid State Sci.* **2009**, *11*, 1319–1324.
24. Qiu, G.; Wang, Q.; Nie, M. Polypyrrole-Fe_3O_4 Magnetic Nanocomposite Prepared by Ultrasonic Irradiation. *Macromol. Mater. Eng.* **2006**, *291*, 68–74.
25. Turcu, R.; Pana, O.; Nan, A.; Craciunescu, I.; Chauvet, O.; Payen, C. Polypyrrole Coated Magnetite Nanoparticles from Water Based Nanofluids. *J. Phys. D: Appl. Phys.* **2008**, *41*, 245002.
26. Wuang, S. C.; Neoh, K. G.; Kang, E.-T.; Pack, D. W.; Leckband, D. E. Synthesis and Functionalization of Polypyrrole-Fe_3O_4 Nanoparticles for Applications in Biomedicine. *J. Mater. Chem.* **2007**, *17*, 3354–3362.
27. Zhang, H.; Zhong, X.; Xu, J.-J.; Chen, H.-Y. Fe_3O_4/Polypyrrole/Au Nanocomposites with Core/Shell/Shell Structure: Synthesis, Characterization, and Their Electrochemical Properties. *Langmuir* **2008**, *24*, 13748–13752.
28. Zhang, Z.; Li, Q.; Yu, L.; Cui, Z.; Zhang, L.; Bowmaker, G. A. Highly Conductive Polypyrrole-Fe_2O_3 Nanospheres with Good Magnetic Properties Obtained through an Improved Chemical One-Step Method. *Macromolecules* **2011**, *44*, 4610–4615.
29. Sun, Z. C.; Geng, Y. H.; Li, J.; Jing, X. B.; Wang, F. S. Chemical Polymerization of Aniline with Hydrogen Peroxide as Oxidant. *Synth. Met.* **1997**, *84*, 99–100.
30. Sun, H.; Shen, X. S.; Yao, L.; Xing, S. X.; Wang, H.; Feng, Y. H.; Chen, H. Y. Measuring the Unusually Slow Ionic Diffusion in Polyaniline *via* Study of Yolk-Shell Nanostructures. *J. Am. Chem. Soc.* **2012**, *134*, 11243–11250.
31. Gill, M. T.; Chapman, S. E.; DeArmitt, C. L.; Baines, F. L.; Dadswell, C. M.; Stamper, J. G.; Lawless, G. A.; Billingham, N. C.; Armes, S. P. A Study of the Kinetics of Polymerization of Aniline Using Proton NMR Spectroscopy. *Synth. Met.* **1998**, *93*, 227–233.
32. Kudoh, Y. Properties of Polypyrrole Prepared by Chemical Polymerization Using Aqueous Solution Containing $Fe_2(SO_4)_3$ and Anionic Surfactant. *Synth. Met.* **1996**, *79*, 17–22.
33. Gao, X. H.; Cui, Y. Y.; Levenson, R. M.; Chung, L. W. K.; Nie, S. M. *In Vivo* Cancer Targeting and Imaging with Semiconductor Quantum Dots. *Nat. Biotechnol.* **2004**, *22*, 969–976.
34. Zrazhevskiy, P.; Sena, M.; Gao, X. H. Designing Multifunctional Quantum Dots for Bioimaging, Detection, and Drug Delivery. *Chem. Soc. Rev.* **2010**, *39*, 4326–4354.
35. Jorgensen, M.; Norrman, K.; Krebs, F. C. Stability/Degradation of Polymer Solar Cells. *Sol. Energy Mater. Sol. Cells* **2008**, *92*, 686–714.
36. Manceau, M.; Bundgaard, E.; Carle, J. E.; Hagemann, O.; Helgesen, M.; Sondergaard, R.; Jorgensen, M.; Krebs, F. C. Photochemical Stability of π-Conjugated Polymers for Polymer Solar Cells: A Rule of Thumb. *J. Mater. Chem.* **2011**, *21*, 4132–4141.
37. O'Donnell, M.; Skovoroda, A. R.; Shapo, B. M.; Emelianov, S. Y. Internal Displacement and Strain Imaging Using Ultrasonic Speckle Tracking. *IEEE Trans. Ultrason. Ferroelectr. Freq. Control* **1994**, *41*, 314–325.
38. Qu, M.; Mallidi, S.; Mehrmohammadi, M.; Truby, R.; Homan, K.; Joshi, P.; Chen, Y.-S.; Sokolov, K.; Emelianov, S. Magneto-Photo-Acoustic Imaging. *Biomed. Opt. Exp.* **2011**, *2*, 385–396.
39. Meyskens, F. L.; Thomson, S. P.; Moon, T. E. Quantitation of the Number of Cells within Tumor Colonies in Semisolid Medium and Their Growth as Oblate Spheroids. *Can. Res.* **1984**, *44*, 271–277.